1 AN AUTONOMOUS MICROCHIP FOR REAL-TIME, LABEL-FREE IMMUNE CELL 2 **ANALYSIS** 3 4 A K M Arifuzzman a, , Norh Asmare a, , Tevhide Ozkaya-Ahmadov a, Ozgun Civelekoglu a, Ningquan Wang a, A. Fatih Sarioglu a, b, c, * 5 6 ^a School of Electrical and Computer Engineering, Georgia Institute of Technology, Atlanta, GA, 7 30332, USA 8 ^b Parker H. Petit Institute for Bioengineering and Bioscience, Georgia Institute of Technology, 9 Atlanta, GA, 30332, USA 10 ^c Institute for Electronics and Nanotechnology, Georgia Institute of Technology, Atlanta, GA, 11 30332, USA 12 13 † These authors contributed equally to this work 14 * Correspondence should be addressed to A.F.S. (<u>sarioglu@gatech.edu</u>) 15 16 **ABSTRACT** 17 Characterization of cell populations and identification of distinct subtypes based on surface markers are needed in a variety of applications from basic research and clinical assays to cell 18 19 manufacturing. Conventional immunophenotyping techniques such as flow cytometry or 20 fluorescence microscopy require immunolabeling of cells, expensive and complex 21 instrumentation, skilled operators, and are therefore incompatible with field deployment and 22 automated cell manufacturing systems. In this work, we introduce an autonomous microchip that 23 can electronically quantify the immunophenotypical composition of a cell suspension. Our 24 microchip identifies different cell subtypes by capturing each in different microfluidic chambers 25 functionalized against the markers of the target populations. All on-chip activity is electronically monitored by an integrated sensor network, which informs an algorithm determining 26 27 subpopulation fractions from chip-wide immunocapture statistics in real time. Moreover, optimal 28 operational conditions within the chip are enforced through a closed-loop feedback control on 29 the sensor data and the cell flow speed, and hence, the antibody-antigen interaction time is 30 maintained within its optimal range for selective immunocapture. We apply our microchip to analyze a mixture of unlabeled CD4+ and CD8+ T cell sub-populations and then validated the 31 32 results against flow cytometry measurements. The demonstrated capability to quantitatively 33 analyze immune cells with no labels has the potential to enable not only autonomous biochip-34 based immunoassays for remote testing but also cell manufacturing bioreactors with built-in, adaptive quality control. 35 36 37 **Keywords:** flow cytometry, T-cell immunophenotyping, sensor network, electronic cytometry,

1

38

39

40

41

autonomous microfluidics.

1. INTRODUCTION

- 2 A special set of proteins and carbohydrates known as cell surface antigens, or markers, are
- 3 expressed on the cell membrane of cells (Kalina et al., 2019; Zola et al., 2007). These markers
- 4 present a rich and unique set of information about a cell, including health, age, growth, stage of
- 5 differentiation and so on (Goodwin et al., 2020; Jensen et al., 2016; Trusler et al., 2018). In the
- 6 case of immune cells, surface markers have been employed extensively to identify to which
- 7 subpopulation a cell belongs (Brown & Greaves, 1974; Priyadarssini et al., 2016). Quantifying
- 8 the prevalence of immune cell types within a sample forms the basis for many types of
- 9 diagnoses, and underpins a wide variety of standard clinical practices, ranging from clinical trial
- 10 qualification to drug development. Beyond these fields, immunophenotyping has been used to
- 11 diagnose immunodeficiency disorders(Bright et al., 2013; Gutierrez et al., 2018; Mishra et al.,
- 12 2014), perform subclassification of leukemia and lymphoma (Burger et al., 1999; Chiaretti et al.,
- 13 2014; Comazzi & Gelain, 2011), monitor the immune system health in HIV patients (Barnett et
- 14 al., 2008; Gojak et al., 2019) and those undergoing immunosuppressive therapy (Furlanetto et al.,
- 15 2017; Spec et al., 2016), to mention a few.
- 16 Multicolor flow cytometry has thus far served as the gold standard for immunophenotype
- measurements due to its unique ability to process large populations of cells and quantify the 17
- expression level of multiple surface markers simultaneously at the single cell level (Baumgarth 18
- 19 & Roederer, 2000; Finak et al., 2016). In this process, cells are first pre-labeled with specific
- 20 antibodies that have been conjugated with fluorochromes and then interrogated under laser
- 21 illumination as they flow in a single file through an aperture (Cho et al., 2010). While
- 22 expressions of different membrane antigens from individual cells can be rapidly and precisely
- 23 measured from the fluorescence emission intensity, flow cytometry is a specialized and laborious
- 24 technique that can only be implemented in centralized research and clinical laboratory settings
- 25 (Abraham & Aubert, 2016; Saeys et al., 2016), where the assay complexity, high operational
- 26 cost, and large instrumental footprint as well as employing skilled operators could be justified
- 27 (Grant et al., 2021).
- 28 Seeking to create low-cost, portable cell immunophenotyping assays, researchers have developed
- 29 microchip-based technologies. Typically, such systems drive a cell suspension through an
- 30 antibody-functionalized microchip which in turn screens the cell population constituents using
- 31 immunoaffinity as the discriminatory mechanism (Y. Liu et al., 2014; Qasaimeh et al., 2017;
- 32 Vickers et al., 2012). Though most of the implementations of this approach relied on microscopy
- 33 for measurements (Huang et al., 2012; M Weerakoon-Ratnayake et al., 2020; Zhang et al., 2018),
- 34 other techniques that integrated sensing elements within the microchip for on-chip quantification
- 35 of the population constituents have also been demonstrated (Civelekoglu et al., 2019;
- 36 Civelekoglu et al., 2022; R. Liu et al., 2020). One such work reports a microfluidic device that
- 37 electrically counts CD4+ and CD8+ lymphocytes present within a whole blood sample after
- lysing the erythrocytes on the chip (Watkins et al., 2013). Another approach, known as the 38
- 39 electronic antibody microarray, utilizes a set of microfluidic capture chambers that have each
- 40 been functionalized against different antigens present on target subpopulations of a given
- 41 sample. The capture statistics are collected using an embedded electrical sensor network for
- 42 combinatorial analysis of multiple antigens at the population level (R. Liu et al., 2019). While
- 43 successfully achieving portability, these miniaturized microfluidic systems require user
- 44 intervention during runtime to keep the operational conditions within favorable bounds

- 1 (Civelekoglu et al., 2022; Wang et al., 2021). Without intervention, process components that
- 2 fluctuate over time such as sample concentration, size and speed might hinder device operation
- 3 or compromise the accuracy of the assay, rendering these approaches unsuitable for use in
- 4 applications like cell manufacturing processes, which require automated, continuous, closed-
- 5 system conditions.
- 6 We present here, an autonomous microchip-based immunoassay that continuously updates
- 7 runtime parameters to maintain optimal operation conditions on the analytical chip for cell
- 8 analysis. To achieve this capability, our work combines microfluidics, integrated on-chip
- 9 sensors, computation and real time feedback control. Specifically, the presented microchip
- 10 utilizes a multi-chamber immunocapture scheme that separates cell subpopulations by capturing
- them based on their surface markers and an integrated electrical sensor network to quantify the
- capture statistics (Fig. 1a). The readout produced by the sensor network is analyzed by our
- custom-built deep learning algorithms to compute population-level insights. These algorithms
- also inform a runtime feedback control algorithm that continually monitors the cell flow
- dynamics and updates the sample drive pressure to maintain optimal cell flow conditions for
- 16 immunocapture.

2. MATERIAL AND METHODS

19 20

2.1. Chemicals and materials

- 21 APTES was purchased from Gelest, Inc. (Morrisville, PA), Neutravidin and BSA were purchased
- from Thermo Scientific (Rockford, IL), Glutaraldehyde, and trichloro(octyl)silane were purchased
- from Sigma-Aldrich (St. Louis, MO), 200 proof ethanol was purchased from Decon Labs, Inc.
- 24 (Kings of Prussia, PA), 1 × PBS was purchased from Mediatech (Manassas, VA), all chemicals
- are analytical grade. All water used for the experiment was deionized (DI) water.
- 26 FITC anti-CD4 antibody (OKT4 clone), APC anti-CD8 antibody (SK1 clone), Biotin anti-CD4
- 27 antibody (SK3 clone), Biotin anti-CD8 antibody (SK1 clone) and APC anti-CD33 (WM53 clone)
- antibody were all purchased from Biolegend (San Diego, CA).
- 29 Density gradient medium LymphoprepTM (Catalog #07801), EasySepTM Buffer (Catalog
- 30 #20144), EasySepTM Human Naïve CD4+ T Cell Isolation Cocktail II (Catalog # 17555), Human
- Naïve CD8+ T Cell Isolation Cocktail II (Catalog # 17968), polystyrene round-bottom tube
- 32 (Catalog # 38007), EasySepTM Magnet (Catalog # 18000), SepMateTM-50 (IVD) (Catalog #
- 33 85450) and ImmunoCultTM-XF T Cell Expansion Medium (Catalog # 10981) were all purchased
- 34 from STEMCELL Technologies (Vancouver, Canada).
- Human Peripheral Blood CD4+CD45RA+ T Cells, Frozen (Catalog # 70029; Lot # 2206403013)
- and Human Peripheral Blood CD8+CD45RA+ T Cells, Frozen (Catalog # 70030; Lot #
- 37 200180505C, 200173103C) were purchased from STEMCELL Technologies (Vancouver,
- 38 Canada).
- 39 4-inch silicon wafers were purchased from UniversityWafer, Inc. (South Boston, MA), SU-8
- 40 2000 series photoresist was purchased from MicroChem (Westborough, MA), NR9-1500PY

negative photoresist was purchased from Futurrex, Inc. (Franklin, NJ), polydimethylsiloxane (PDMS) elastomer Sylgard 184 was purchased from Dow Corning (Auburn, MI).

2 3 4

1

2.2. Fabrication

- 5 The microchip was fabricated using soft lithography and surface micromachining techniques. To
- 6 fabricate the microfluidic layer, at 15 μm thick negative photoresist SU-8 (SU-8 2015,
- 7 MicroChem) was spin coated onto a silicon wafer. The design pattern was transferred to the
- 8 resist layer by exposing the resist layer using a maskless aligner (MLA-1500, Heidelberg) and
- 9 then, the uncured photoresist was developed using SU-8 developer and treated with
- trichloro(octyl)silane in a desiccator for 8 h. Then, a mixture of PDMS elastomer and its
- 11 crosslinker (Sylgard 184 kit, Dow Corning) was prepared at a 10:1 ratio (by weight) and poured
- onto the mold, degassed and cured for 4 h at 65°C. Finally, the cured PDMS was peeled off and
- 13 cut into individual chips. To fabricate the electrical sensor network, 1.5 μm thick negative
- photoresist (NR9-1500PY, Futurrex) was spin coated onto a 2-inch by 3-inch glass microscope
- slide (6101, Premiere). The electrode pattern was transferred to the resist layer using a maskless
- aligner (MLA-1500, Heidelberg) and developed using photoresist developer (RD6 developer,
- 17 Futurrex). Then, the glass slides were treated with reactive ion etcher for descumming followed
- by e-beam deposition of 20 nm-thick Cr and 250 nm-thick Au film stacks. The sacrificial
- 19 photoresist layer was lifted-off by submerging the glass substrate into an acetone bath under mild
- sonication. Finally, the PDMS layer and the glass substrate were treated with oxygen plasma for
- 21 1 min for surface activation before being aligned under microscope and bonded at 65 °C to create
- the final microchip.

2324

2.3. Capture chamber modification for CD4+ and CD8+ T cells

- Our microchip was functionalized using avidin-biotin functionalization protocol. First, the
- 26 microfluidic device was wetted with ethanol within 10 mins of the oxygen plasma assisted
- 27 PDMS-glass bonding. Then, APTES with ethanol (3% v/v) was introduced to the device.
- Following 1 h incubation at room temperature, the microchip was washed with ethanol and
- incubated at 110°C in a vacuum oven. Next, the microchip was washed with DI water and
- infused with a glutaraldehyde solution in DI water (3% v/v). After 1 h incubation at room
- 31 temperature, the microchip was washed with DI and PBS before introducing a 1 mg/mL solution
- of neutravidin in PBS into the microchip and incubating for 4 h. The microchip was then rinsed
- with PBS and incubated with a solution of 3% BSA blocking buffer and 1.5 mg/mL glycine for 1
- 34 h to block nonspecific binding sites. Once complete, the microchip was washed with PBS and
- 35 capture chambers were incubated with biotin conjugated antibodies for 2 h. Finally, the
- microchip was washed with PBS to remove unbound antibodies.

3738

2.4. Measurement of false positive capture rate

- 39 To minimize false positive capture in the capture chamber, bovine serum albumin (BSA) and
- 40 glycine were used. To find the false positive capture rate, a single-chamber microchip was
- assembled and functionalized the capture chamber with anti-CD4 antibody, BSA and glycine.
- Then, a mixed population of CD4+ T cells and CD8+ T cells were driven through the
- functionalized device at optimal flow speed. The false positive capture rate was calculated as (a)
- 44 the total number of CD8+ T cells immobilized in the anti-CD4 functionalized chamber divided

by (b) the total number of cells processed through the microchip. To determine (a), the microchip was post-labeled with FITC anti-CD4 antibody to first distinguish the correctly captured CD4+ expressors in the chamber. This count was then subtracted from the total captured cells to determine the population of incorrectly captured, CD4-expressors present in the chamber. To determine (b), the sum of the total number of cells captured in the chamber and the total number of uncaptured cells present in the liquid ejected from the microchip were computed.

2.5. T cell isolation from whole blood

30 mL blood samples were collected from healthy donors according to an IRB-approved protocol. All blood samples were collected in BD EDTA tubes in order to prevent coagulation and placed on a rocker at room temperature. Blood samples were always processed within 4 h of the blood withdrawal. To successfully separate naïve CD4+ and CD8+ T cells from whole blood sample, peripheral blood mononuclear cells (PBMC) were first isolated from whole blood using density gradient medium (Lymphoprep, STEMCELL Technologies). Then, naïve CD4+ and CD8+ T cells were isolated from PBMC using the immunomagnetic negative selection process. This procedure involves labelling unwanted PBMC cells with antibody complexes and magnetic particles (EasySepTM Human Naïve CD4+ T Cell Isolation Kit II, EasySepTM Human Naïve CD8+ T Cell Isolation Kit II, STEMCELL Technologies) and then separating the magnetically labelled cells using a magnet (EasySepTM Magnet, STEMCELL Technologies) followed by pouring the desired cell population (naïve CD4+ and CD8+ T cell) into a new tube. The entire process of isolating T cells from whole blood took ~2.5 h.

2.6. Preparation of commercial T-cell samples for processing

First, frozen human naïve CD4+ T cells (STEMCELL Technologies) and naïve CD8+ T cells (STEMCELL Technologies) were thawed using manufacturer protocol in ~30 mins. The initial concentration of both cell samples was 5×10^6 cells/mL. Then, both cell samples were diluted to obtain stock samples each with a concentration of 1×10^6 cells/mL. If a heterogeneous sample that contained both T cell types was required for an experiment, a final volume and mixing ratio were first determined, then the appropriate volumes of cells were taken from the previously prepared CD4+ and CD8+ stock solutions and mixed in the same sample tube. For the BSA concentration experiment, the final volume was $400~\mu\text{L}$ with a 1:1 mixing ratio. For the subpopulation analysis experiment, three samples were prepared, each with a final volume of $400~\mu\text{L}$ and mixing ratios of 1:1, 1:2, and 2:1.

2.7. Experimental setup

The cell suspension was loaded into a reservoir, which is a 1 mL syringe barrel sealed with a custom-made airtight cap. This cap is ported to accept a 1.5 mm diameter tube running from the pressure pump. The electrical sensor network is excited with a 2 Vpp sinusoidal wave at 550 kHz through the input pads, and the output currents at the positive and negative pads were amplified via transimpedance amplifiers before being sampled by the lock-in amplifier (HF2LI, Zurich Instruments). The lock-in amplifier output was sampled into a computer using a standalone analog to digital converter (PCIe-6361, National Instruments) to be passed on to the algorithm suite for real-time analysis of cell events on the microchip.

2.8. Flow cytometry validation

- 2 The experimental results were verified by analyzing the sample processed by our microchip in a
- 3 flow cytometer. The sample was labeled with FITC anti-CD4 antibody (OKT4 clone, Biolegend)
- 4 and APC anti-CD8 antibody (SK1 clone, Biolegend). This labeled sample was introduced into
- 5 the flow cytometer (LSR-II, BD Biosciences) and subsequently, the laser power values were
- 6 configured for optimal measurement (FSC: 275 V, SSC: 250 V, FITC: 390 V and APC: 390 V).
- 7 The processing was halted after 10,000 events were recorded for every sample. Finally, FlowJo
- 8 (FlowJo, LLC) software was used to analyze the flow cytometry data.

9 10

1

3. RESULTS

11 12

13

3.1. System overview and microchip design

- Our autonomous microchip-based immunoassay consisted of a microchip, a signal processing
- 14 scheme and a feedback control loop. The microchip itself was composed of fluidic and electrical
- 15 components (Fig. 1b). The microfluidic layer was made out of polydimethylsiloxane (PDMS)
- 16 that accommodated the cascaded cell capture chambers. The cells flowed through those
- 17 chambers sequentially and interacted with the different types of antibodies, resulting in the target
- 18 cell subpopulation of each chamber getting immobilized on contact. An electrical sensor network
- 19 based on the Microfluidic CODES (R. Liu et al., 2016, 2017) platform monitored cell flow at
- 20 strategically placed locations. Specifically, a count was kept of every cell that entered the
- 21 microchip, exited the first chamber to enter the second, and exited the second channel to leave
- 22 the microchip. Using these counts in a mass balance equation revealed the antigen-positive cell
- 23 count in each capture chamber. A sensor was defined as a series of interdigitated electrode pairs,
- 24 comprised of positive and negative output electrode fingers, which served as current sinks, and a
- 25 common input electrode, which served as the current source, that meandered throughout the
- length of the sensor and formed pairs with the output electrodes. All of the electrode fingers were 26
- 27 5 μm wide and were spaced apart by 5 μm (Fig. 1b). Each sensor in the network had 15 pairs and
- 28 generated a waveform with as many peaks of varying polarities effectively producing a unique
- 29 code for each sensor. The specific sequence of these polarities followed the prescribed physical
- 30 ordering of input-output electrode finger pairs, and ultimately determined the unique shape of the
- 31 generated waveform. Our system used the uniqueness of each waveform during signal
- 32 processing to determine from which sensor a particular waveform originated.
- 33 The dimensions of the microfluidic pathways were optimized based on the target cell population,
- 34 which in this case were naïve T cells that have an average diameter of ~7 µm. The capture
- 35 chambers measured 7 mm in length and 5 mm in width and featured 60 µm diameter pillars
- 36 patterned with a 72 um pitch (Fig. 1b). The channel height over the capture region was designed
- 37 to be 15 µm. The pillar dimensions and pitch were optimized to maximize interaction between
- 38 the cell and the antibody coated pillars while still allowing sufficient clearance to prevent
- 39 clogging. The pillars also served a secondary function of structurally supporting the ceiling of
- 40 the chamber against collapse. The capture chambers also featured a set of auxiliary
- 41 functionalization ports and channels located close to the inlet and outlet of each chamber. Each
- 42 of these auxiliary channels featured a diamond-shaped, micropillar array-based particulate filter
- 43 to prevent pollutants entering the capture chambers during the multi-step functionalization
- 44 process. This setup allowed exclusive delivery of functionalization reagents to the desired
- chamber. Following the functionalization process, the auxiliary ports were sealed to prevent 45

leakage during the assay operation, and the microchip was interfaced via a single fluidic inlet and outlet.

2 3 4

5

6

7

8

9

10

11 12

13

14

15

1

In operation, cells, flowing through the microchip, passed over each of the sensors embedded in the channel floor. The output of the whole sensor network was a differential electrical waveform that was first amplified by a pair of transimpedance amplifiers, processed by the lock-in amplifier (LIA) before being sampled into the computer via an analog to digital converter (ADC) (Materials and methods). The digitized sensor waveform was then processed by a deep learning model in real time to compute subpopulation fractions. Frequencies of different subpopulations were quantitatively determined by analyzing the differential cell counts at the entry and exit of each chamber. Cell speed was continuously computed from the sensor network data and was used to concurrently inform the feedback control system on the instantaneous operational status of the microchip. We used the cell speed as a process parameter to actively control the drive pressure and maintain a closed loop (Fig. 1c). This feedback control scheme enabled efficient immunocapture of cells without prior knowledge of the device dimensions and channel fluidic resistance.

16 17 18

3.2. Surface modification and optimization of cell capture parameters

19 To target different subpopulations of T cells, anti-CD4 and anti-CD8 antibodies were

20 immobilized in different cell capture chambers through avidin-biotin chemistry (Materials and

21 methods) via the auxiliary functionalization ports (Fig. 1b). First, the center auxiliary ports of the

22 microchip were used to infuse the reagents common to both chambers, namely, (3-

aminopropyl)triethoxysilane (APTES) glutaraldehyde, neutravidin, BSA and glycine. Then,

24 through the outer two auxiliary ports, the chamber-specific antibodies were infused into the

25 corresponding chambers simultaneously at the same laminar flow rate. The symmetric design of

26 the chambers ensured the chambers were infused equally and neither antibody solution

overflowed its chamber and mixed with the other.

- 28 To investigate the immobilization specificity of the capture antibodies in their designated capture
- 29 chambers, we first functionalized capture chambers with antibodies conjugated with
- 30 fluorophores of dissimilar colors (FITC anti-CD4 antibody and APC anti-CD8 antibody).
- 31 Fluorophore-conjugated antibodies were concurrently delivered to different capture chambers
- 32 and fluorescence emission was analyzed with fluorescence microscopy. Our results confirmed
- that each capture chamber was successfully coated with the desired antibody and that the
- 34 fluorescence signal was uniform across each chamber, suggesting an even coating throughout
- 35 (Fig. 2a). Furthermore, each antibody was confined to their target chambers and had not leaked
- into adjacent chambers.
- We then aimed to determine the optimal antibody concentration for surface functionalization. In
- 38 this process, we functionalized different microfluidic capture chambers by incubating with anti-
- 39 CD4 antibodies at different concentrations (1–50µg/mL) and measured the resulting
- 40 immunocapture efficiencies for CD4+ T cells as a function of incubation antibody concentration
- 41 (Fig. S2). We found the cell immunocapture efficiency to be highly dependent on antibody
- 42 concentration when it is <10μg/mL, while the gains in immunocapture efficiency being minimal
- for antibody concentrations of >25µg/mL, which suggested a saturation of the functionalized
- surface. Based on these results, 25µg/mL was chosen as the optimal antibody concentration for
- surface functionalization and was employed for the rest of the experiments in this work.

1 Next, we investigated the effect of cell flow speed on the immunocapture efficiency. The cell

2 immunocapture efficiency, a performance metric we sought to maximize, is primarily dictated by

- 3 the antibody-antigen interaction time in addition to the affinity between the two. Too high a flow
- 4 speed leads to an inadequately low interaction time, resulting in false negatives in the form of
- 5 uncaptured target T cells. Conversely, too low a flow speed causes non-specific binding,
- 6 resulting in false positives due to non-target cells adhering to chamber surface. To determine the
- 7 optimal flow speed, we processed a homogeneous naïve CD4+ T cell population, under different
- 8 driving pressures and measured the percentage of the total incoming cells that were arrested in
- 9 the capture chamber functionalized with anti-CD4 antibody to calculate capture efficiency. We
- achieved a 93% capture rate at flow speed of 30 μm/ms while increasing the flow speed to 150
- 11 μm/ms led to a reduction in capture rate to 80% (Fig. 2b). The selected operating flow speed was
- 12 60 μm/ms as it exhibited a relatively high (92%) capture rate while crucially avoiding non-
- specific adhesion artifacts and sedimentation issues that the slower flow speeds were prone to.
- To minimize the non-specific adhesion, and hence, to increase the specificity of our assay, we
- investigated blocking the microchip with bovine serum albumin (BSA) and glycine. In order to
- determine the optimal BSA concentration for blocking, we measured false-capture rates of non-
- target cells (CD8+ T cells) in devices functionalized with anti-CD4 antibody, 1.5 mg/mL of
- 18 glycine and different concentrations of BSA (Materials and methods). For samples processed at
- 19 the optimized cell flow speed of 60 μ m/ms, we found that BSA concentrations of < 3% led to
- 20 non-specific capture of CD8+ T cells, leading to false positive results of up to 42%. Increasing
- 21 BSA concentration to 3% reduced non-specific adhesion to < 3% and was chosen as the optimal
- concentration for studies in this paper (Fig. 2c).
- Finally, we tested the specificity of our assay with optimized surface chemistry in a multi-
- 24 chamber configuration. In these experiments, microchips were functionalized either with anti-
- 25 CD4 or anti-CD8 antibody and only at the first capture chamber. The second chamber was
- 26 intentionally left unfunctionalized for all microchips in order to observe non-specific capture.
- When homogeneous populations of naïve CD4+ T cells and naïve CD8+ T cells, each obtained
- from a commercial vendor (Materials and methods), were processed at 60 µm/ms, we observed T
- cells to be captured predominantly (~92% of CD4+ T cells and ~87% of CD8+ T cells) in the
- 30 chamber functionalized with the matching antibody (Fig. 2d and e). Moreover, across different
- 31 microchips, the non-specific capture rate was \sim 3% on average. Considering the fact that the
- 32 samples we process already contained impurities per vendor-provided datasheets (CD4+ T cell
- sample purity: 94% and CD8+ T cell sample purity: 88%), these results demonstrated virtually
- 34 almost all T cells expressing target antigens were captured by the optimized device with minimal
- 35 non-specific capture.

3637

3.3. Real-time determination of cell immunocapture statistics

- 38 To process electrical signals produced by the microchip, we designed a data processing pipeline
- that amplified, digitized and analyzed the waveform in real time (Fig. 3a). The front-end of this
- 40 system was comprised of transimpedance amplifiers that conditioned the signal and passed it
- onto a lock-in amplifier (Materials and methods), which in turn produced the raw signal stream
- 42 (Fig. 3b) and provided it to a digitizer connected to a computer. Once digitized, the signal was
- processed by a suite of algorithms written in Python, starting with automatically extracting valid
- cell events from the raw signal stream which included undesired idle sensor signals as well. This

was done by continuously running a sliding window on the raw signal stream, computing the signal power within the window and saving the windows that exceed a threshold. This threshold was determined using the first 5 seconds of program runtime by aggregating several thousand windows, identifying 100 windows with the lowest powers, and computing their average. This average was designated as the noise floor power, and an empirically determined threshold of 14 dB relative to this noise floor power was used as the threshold for all signals processed. The detected cell event segments were then subject to a boundary refinement routine, where the minor extraneous idle sections of the signal on the leading and trailing ends of the segment are discarded. This routine first identifies the first and last peaks of the signal, then follows outer halves of these peaks until their first inflection points. The segment is trimmed to start and end within these new points.

Next, the refined segment was forwarded to our deep learning model (Wang et al., 2019, 2021) for interpretation (Fig. 3c). The deep learning model could extract the information embedded in the cell signals at a processing throughput exceeding 700 cells/s, a rate that allows real-time operation in practice. Briefly, our model is comprised of two cascaded convolutional neural networks, which are deep learning structures commonly used in signal processing. The first stage, the region proposal network (RPN), designated the temporal location of each cell event by estimating a bounding box for each signature waveform identified in addition to reporting the cell speed. The second stage, the sensor classification network (SCN), performed classification on every bounding box produced by the RPN that preceded it and reported the class, or sensor ID, that corresponds to the waveform. While the functions of these two networks differ, their structure is similar. They both featured 4 convolutional layers expecting input waveforms normalized to 200 samples. The output of the SCN contained three nodes, each of which represented one of the three sensors embedded in the microchip (Fig. 3d). The two outputs of the deep learning model, namely the cell event sensor ID and cell speed were used by the chamber capture counting routine and the feedback control algorithm, respectively.

The final stage in the data processing pipeline mapped each of the aggregated cell event sensor IDs to their corresponding sensor on the microchip and computed the capture rate (Fig. 3d). Each of the three sensors represented counts of a different cell population. The first sensor located nearest to the inlet counted the total population of the processed cells, while the second sensor located at the exit of the first chamber counted the subpopulation that was not immobilized in the first chamber and was therefore a negative expressor of that target antigen, and finally the third sensor located at the exit of the second chamber counted the subpopulation that was not immobilized in the second chamber. In a microchip where the first and second chambers have been functionalized with anti-CD4 and anti-CD8 antibodies, respectively, the count difference between the first and second sensor represented the CD4+ fraction of the population, the count difference between the second and third sensor represented the CD4- CD8+ fraction of the population and finally, the count difference between the first and third sensor represented the CD4- CD8- fraction of the total population.

3.4. Closed-loop feedback control of the cell-flow speed for optimal immunocapture

In order to autonomously maintain an optimal antibody-antigen interaction time for a given cell population, we developed a feedback control algorithm that modulates the drive pressure of the pressure pump pushing the cell sample based on the measured cell speed over the sensor network.

The control algorithm ran in real time, concurrent with the capture statistics algorithm, and continuously factored in new cell measurements while making necessary adjustments to the pressure pump over a USB connection (Fig. 4a). The control algorithm received a segmented cell event that has been baseline removed and determined the signal length. The cell speed is then computed using the known physical dimension of the sensor and signal sample rate. Every such cell speed measurement was added to a moving average of 9 cell events. If this average exceeded the target by 10%, the drive pressure was reduced. Conversely, if this average was below the target by 10%, the drive pressure was increased.

We abstracted the control routine into a plant and feedback controller scheme (Fig. 4b). The programmable pressure pump, sensors and signal processing components comprise the plant and produce the measured process variable, the average cell speed (y(t)). The operational target of the feedback control system was to modulate the input, in this case the pump drive pressure, such that the average cell speed approaches the target setpoint (r(t)). To accomplish this, the discrepancy between the measured cell speed and the setpoint is computed as the error (e(t)) and the feedback controller continually attempts to minimize this value by executing an adequate correction value (u(t)) to the control input. Here, we implemented a proportional controller, which adjusted the control input based on a weight applied to the error. As such, the adjustment value passed to the pressure pump was given by:

1 2

$$u(t) = Ke(t),$$

where *K* was the feedback gain. *K* was determined heuristically to be 0.35, avoiding excessively low values that resulted in prolonged time before converging on the target, and excessively high values which led to overshooting (Fig. S1).

We were able to directly use the cell flow speed in the feedback control system to modulate the drive pressure since these two parameters exhibited a linear, monotonic relationship with the proportionality constant determined by the microchip hydraulic resistance (Fig. 4c). Every time the average cell speed was updated, which occurred at every cell event detection, the error between the measured and targeted cell speed was computed, and the feedback controller sent an update to the pressure pump if needed.

We characterized the responsiveness of the feedback control loop by implementing a non-static setpoint and monitoring the controller's output (Fig. 4d). We programmed the cell speed setpoint to follow a prescribed pattern, namely a linear ramp increasing from 35 μ m/ms to 60 μ m/ms, and found that the controller was able to follow it successfully. Finally, we evaluated the effect of disabling the feedback control algorithm on the capture rate (Fig. 4e). The system was run with a sample of homogeneous CD4+ T cells and the instantaneous capture rate was computed for every 16 cell events. Once the average instantaneous capture rate stabilized at ~88%, the feedback control algorithm was disabled and the system state was perturbed by abruptly increasing drive pressure to 950 mbar. The capture rate dropped to ~63% as a result. The feedback control algorithm was then re-enabled and autonomously brought the average instantaneous capture rate back to its previous ~88%. These results functionally demonstrated the ability of the assay to operate under optimal conditions irrespective of external perturbations.

3.5. Immunoanalysis of heterogenous T cell populations

- 2 We evaluated the performance of the complete system consisting of the developed hardware and
- 3 software by processing heterogenous samples of mixed T cell populations, specifically naïve
- 4 CD4+ and CD8+ T cells isolated from whole blood (Materials and methods). To discriminate
- 5 between different T cell subpopulations, our microchip was functionalized such that the first
- 6 chamber would capture exclusively CD4+ T cells, the second chamber would capture CD8+ T
- 7 cells and the cells/particles expressing neither were evacuated from the device (Fig. 5a). Because
- 8 CD4 and CD8 are rarely co-expressed by T cells in peripheral blood (Bohner et al., 2019;
- 9 Overgaard et al., 2015), our cascaded capture chambers effectively separated the two T cell
- populations through immunocapture. In fact, we confirmed that both capture chambers were
- capturing their intended target cell populations by labeling captured cell population on the
- microchip with different-colored fluorophores (FITC anti-CD4 antibody and APC anti-CD8
- antibody) and imaging them with fluorescence microscopy (Fig. 5a). Next, we tested the
- 14 feedback controller's performance in maintaining the cell speed upon startup. The program was
- 15 first provided with a cell speed target and the allowed tolerance about this target, then launched
- with an initial drive pressure of 500 mbar. The average cell speed was continuously computed as
- the first few cells passing through the microchip were detected. The feedback control algorithm
- gradually reduced the drive pressure until the average cell speed met the target and fluctuations
- stayed within the target bounds. The optimal drive pressure was reached after acquiring signals
- from observing 31 cell events and the target cell speed of 60 µm/ms was met, after which cell
- 21 capture statistics collection began (Fig. 5b). The whole process of analyzing ~12,000 T-cells and
- 21 capture statistics confection began (Fig. 50). The whole process of analyzing ~12,000 1-cens and
- 22 computing the capture statistics required ~30 mins.
- 23 To test the accuracy of our system, we processed calibrated suspensions prepared by mixing
- commercially acquired naïve CD4+ T cells and naïve CD8+ T cells at different ratios of 1:1, 1:2,
- and 2:1 (Materials and methods). After processing each mixed sample through identically
- designed microchips, we found that the immunophenotype composition ratio reported by our
- 27 system was in close agreement with the implemented mixing ratios (Fig. 5c). The discrepancy
- between our results and the nominal mixing ratio were primarily attributed to impurity of
- 29 prepared T cell populations that resulted from lysed or dead cells, non-target particles, and
- impurity of the source samples themselves. Our conclusions are supported by the fact that the
- used CD4+ T cell and CD8+ T cell samples had manufacturer-reported purities of 94% and 93%,
- 32 respectively.

- Finally, we benchmarked our autonomous immunoanalysis system against a commercial
- 34 fluorescence-based flow cytometer. For flow cytometry analysis, samples, prepared by mixing
- 35 CD4+ and CD8+ T cells at a 1:1 ratio, were labeled with fluorophore-conjugated antibodies
- against the same set of target antigens for flow cytometry analysis (Materials and methods).
- Flow cytometry measurements were then gated based on surface expression for T cell
- 38 classification to calculate the frequency of each T cell subpopulation (Fig. 5d). The percentage of
- 39 CD4+CD8- T cells, CD4-CD8+ T cells, and CD4-CD8- expressors were 48.3%, 46.8%, and
- 40 4.1% respectively as per flow cytometry results. These results were in good agreement with
- 41 those from our immunoanalysis system, which reported 49.3%, 43.8% and 6.9% as the
- 42 frequencies of aforementioned immunophenotypes. Considering the flow cytometry data as the
- 43 ground truth, these results amounted to an average of < 6% error rate (n=3), effectively
- representing an accuracy of >94% for our biosensor (Fig. 5d). We attributed our measurement
- errors to several factors: 1) our immunocapture-based technique is a completely different sensing

modality from the laser-scatter technique that a flow cytometer is based on. This difference leads to dissimilar discrimination criteria and will inevitably not match perfectly, 2) the multi-step sample preparation process will unavoidably lead to cell loss and inclusion of non-target cell particles, e.g., lysed residues and dead cells.

4. DISCUSSION

We have demonstrated a fully electronic, autonomous immunoanalysis microchip that performs quantification of immune cell subtypes in a sample. A key feature of our approach is its innate flexibility in terms of both scaling and use case. While we have shown immunophenotyping for CD4+ and CD8+ T cells, a microchip that can target more or a different set of surface markers can be readily created by employing different antibodies or more capture chambers in various arrangements. Due to the already multiplexed nature of the Microfluidic CODES sensor network we utilize, no additional signal input and output ports needed be designed for those expanded systems. Instead, patterning additional sensors around the additional chambers is the only change necessary.

Autonomous operation through a feedback loop is another important feature of the presented system. Our platform can readily by adapted for use with process parameters other than our demonstrated one, i.e., drive pressure. For instance, instead of using the measured cell speed to modulate drive pressure, the feedback control algorithm can be adapted to use measured subpopulation ratios to modulate process parameters like sample concentration. While we have reported an immunophenotype application, the central components of this platform, namely the sensor network and accompanying algorithm suite, microfluidic channel and feedback scheme are abstracted enough to be readily adaptable to other applications that utilize a variety of process parameters.

Finally, our approach presents several advantages over existing immunophenotype techniques. First, unlike traditional approaches which require the sample to be prelabeled with fluorophoreconjugated antibodies, our microchip accepts unlabeled immune cells directly isolated from whole blood. Not only does this shorten assay time, but also makes immunophenotyping available for applications where sample pre-labeling is not feasible. Second, our fully-electronic sensing scheme allows the use of low-cost, commercially available components and circuits which reduces system cost and complexity. While other electronic assays use cell size and electrical properties to indirectly perform cytometry, ours can also access and utilize wellestablished and specific biochemical markers. This brings with it more reliability and compatibility with existing techniques for cell interrogation. Third, our automated processing eliminates errors that clinical cytometry often suffers from, which is primarily caused by variability in operators, laboratory conditions and result interpretation. Lastly, the inherent adaptability of our platform for use with different configurations and operational settings means the ability to perform immunophenotyping can be delivered beyond central laboratories. The system we have presented here has the potential to serve in the next generation of field-deployed analysis tools by leveraging its ability to perform autonomous, label free, real-time analysis.

5. CONCLUSION

 We demonstrate a microchip-based immunoassay to screen T cells for discriminating between different subpopulations based on cell surface markers. To minimize human intervention during operation, the system was designed to run in an automated, closed-loop manner and leveraged a deep-learning based feedback system to enact prompt and accurate adjustments to the runtime parameters during operation. Performing these corrections automatically realizes unique and important advantages over traditional immunophenotyping methods. Specifically, our technique requires no pre-labeling of the sample before running the assay, and crucially, the adaptive, closed-loop operation frees our system from common errors in clinical cytometry primarily caused by handling and environmental variations. While we have demonstrated a proof-ofconcept implementation that targets two surface markers, the scalable nature of our immunocapture scheme enables a straightforward application of our approach to target a multitude of surface markers by simply adding chambers to the design and functionalizing them accordingly. Furthermore, the measurement throughput can be further increased by revising the fluidic design to lower the hydraulic resistance. We believe that our low-cost platform that delivers immunophenotyping capabilities in a disposable package will be invaluable to clinical applications, cell manufacturing, and resource limited settings at the point of care.

CREDIT AUTHORSHIP CONTRIBUTION STATEMENT

A K M Arifuzzman: Conceptualization, Methodology, Investigation, Validation, Writing — original draft, Writing — review & editing. Norh Asmare: Conceptualization, Methodology, Software, Investigation, Writing — original draft, Writing — review & editing. Tevhide Ozkaya-Ahmadov: Resources. Ozgun Civelekoglu: Resources. Ningquan Wang: Resources. A. Fatih Sarioglu: Conceptualization, Methodology, Supervision, Writing, — original draft, Writing — review & editing, Funding acquisition.

DECLARATION OF COMPETING INTEREST

The authors declare that they have no known competing financial interests or personal relationships that could have appeared to influence the work reported in this paper.

ACKNOWLEDGEMENTS

This work was supported by NSF Engineering Research Center for Cell Manufacturing Technologies (CMaT) seed grant, the Arnold and Mabel Beckman Foundation, USA (Beckman Young Investigator Award to A.F.S.) and the National Science Foundation, USA (Award No. ECCS 1752170). The authors would also like to thank the Georgia Tech Stamps Health Services staff for their help in withdrawing blood samples from healthy volunteers.

REFERENCES

- Abraham, R. S., & Aubert, G. (2016). Flow cytometry, a versatile tool for diagnosis and monitoring of primary immunodeficiencies. *Clinical and Vaccine Immunology*, 23(4), 254–271.
- Barnett, D., Walker, B., Landay, A., & Denny, T. N. (2008). CD4 immunophenotyping in HIV
 infection. *Nature Reviews Microbiology*, 6(11).
- Baumgarth, N., & Roederer, M. (2000). A practical approach to multicolor flow cytometry for immunophenotyping. *Journal of Immunological Methods*, 243(1-2), 77-97.
- Bohner, P., Chevalier, M. F., Cesson, V., Rodrigues-Dias, S. C., Dartiguenave, F., Burruni, R.,
 Tawadros, T., Valerio, M., Lucca, I., Nardelli-Haefliger, D., Jichlinski, P., & Derré, L.
 (2019). Double positive CD4+CD8+ T cells are enriched in urological cancers and favor T
 helper-2 polarization. *Frontiers in Immunology*, 10(622).
- Bright, P., Grigoriadou, S., Kamperidis, P., Buckland, M., Hickey, A., & Longhurst, H. J. (2013). Changes in B cell immunophenotype in common variable immunodeficiency: Cause or effect is bronchiectasis indicative of undiagnosed immunodeficiency? *Clinical and Experimental Immunology*, 171(2), 195–200.
- Brown, G., & Greaves, M. (1974). Cell surface markers for human T and B lymphocytes.

 European Journal of Immunology, 4(4), 302-310.
- Burger, R., Hansen-Hagge, T. E., Drexler, H. G., & Gramatzki, M. (1999). Heterogeneity of T-acute lymphoblastic leukemia (T-ALL) cell lines: Suggestion for classification by immunophenotype and T-cell receptor studies. *Leukemia Research*, 23(1), 19-27.
- Chiaretti, S., Zini, G., & Bassan, R. (2014). Diagnosis and subclassification of acute
 lymphoblastic leukemia. *Mediterranean Journal of Hematology and Infectious Diseases*,
 6(1).
- 26 Cho, S. H., Godin, J. M., Chen, C.-H., Qiao, W., Lee, H., & Lo, Y.-H. (2010). Review Article: Recent advancements in optofluidic flow cytometer. *Biomicrofluidics*, *4*(4), 043001.
- Civelekoglu, O., Liu, R., Usanmaz, C. F., Chu, C. H., Boya, M., Ozkaya-Ahmadov, T.,
 Arifuzzman, A. K. M., Wang, N., & Sarioglu, A. F. (2022). Electronic measurement of cell
 antigen expression in whole blood. *Lab on a Chip*, 22(2), 296–312.
- Civelekoglu, O., Wang, N., Arifuzzman, A. K. M., Boya, M., & Sarioglu, A. F. (2022).
 Automated lightless cytometry on a microchip with adaptive immunomagnetic
 manipulation. *Biosensors and Bioelectronics*, 203.
- Civelekoglu, O., Wang, N., Boya, M., Ozkaya-Ahmadov, T., Liu, R., & Sarioglu, A. F. (2019).
 Electronic profiling of membrane antigen expression via immunomagnetic cell
 manipulation. *Lab on a Chip*, 19(14), 2444–2455.
- Comazzi, S., & Gelain, M. E. (2011). Use of flow cytometric immunophenotyping to refine the cytological diagnosis of canine lymphoma. *Veterinary Journal*, 188(2),149–155.
- Finak, G., Langweiler, M., Jaimes, M., Malek, M., Taghiyar, J., Korin, Y., Raddassi, K., Devine, L., Obermoser, G., Pekalski, M. L., Pontikos, N., Diaz, A., Heck, S., Villanova, F.,
- 41 Terrazzini, N., Kern, F., Qian, Y., Stanton, R., Wang, K., ... McCoy, J. P. (2016).
- 42 Standardizing Flow Cytometry Immunophenotyping Analysis from the Human
- ImmunoPhenotyping Consortium. *Scientific Reports*, 6.

- 1 Furlanetto, G., Alegretti, A. P., Farias, M. G., Freitas, P. A. C., Lara, G. M., & Pedrazzani, F. S.
- 2 (2017). Cut-off value for absolute lymphocytes as an alternative for the immunophenotypic
- analysis of CD3+ T cells in the monitoring of immunosuppressive therapy with
- 4 thymoglobulin. *Jornal Brasileiro de Nefrologia : 'orgao Oficial de Sociedades Brasileira e Latino-Americana de Nefrologia*, 39(2), 181–185.
- 6 Gojak, R., Hadžiosmanović, V., Baljić, R., Zečević, L., Ćorić, J., & Mijailović, Ž. (2019).
- 7 CD4/CD8 ratio as a predictor for the occurrence of metabolic syndrome in HIV / AIDS
- patients during 6 months of cART therapy. *Journal of Medical Biochemistry*, 38(4), 489–495.
- Goodwin, J., Laslett, A. L., & Rugg-Gunn, P. J. (2020). The application of cell surface markers to demarcate distinct human pluripotent states. *Experimental Cell Research*, 387(1).
- 12 Gutierrez, M. J., Sullivan, K. E., Fuleihan, R., & Bingham, C. O. (2018). Phenotypic
- characterization of patients with rheumatologic manifestations of common variable
- immunodeficiency. Seminars in Arthritis and Rheumatism, 48(2), 318–326.
- Huang, N. T., Chen, W., Oh, B. R., Fu, J., & Kurabayashi, K. (2012). An integrated microfluidic
- platform for in-situ cellular cytokine secretion immunophenotyping. *Proceedings of the*
- 17 16th International Conference on Miniaturized Systems for Chemistry and Life Sciences,
- 18 *MicroTAS 2012*, 989–991.
- Jensen, C. T., Lang, S., Somasundaram, R., Soneji, S., & Sigvardsson, M. (2016). Identification of Stage-Specific Surface Markers in Early B Cell Development Provides Novel Tools for
- Identification of Progenitor Populations. *The Journal of Immunology*, 197(5), 1937–1944.
- 22 Kalina, T., Fišer, K., Pérez-Andrés, M., Kužílková, D., Cuenca, M., Bartol, S. J. W., Blanco, E.,
- Engel, P., & van Zelm, M. C. (2019). CD maps—dynamic profiling of CD1–CD100 surface expression on human leukocyte and lymphocyte subsets. *Frontiers in Immunology*, 10.
- Liu, R., Arifuzzman, A. K. M., Wang, N., Civelekoglu, O., & Sarioglu, A. F. (2020). Electronic Immunoaffinity Assay for Differential Leukocyte Counts. *Journal of*
- 27 Microelectromechanical Systems, 29(5), 942–947.
- 28 Liu, R., Chu, C. H., Wang, N., Ozkaya-Ahmadov, T., Civelekoglu, O., Lee, D., Arifuzzman, A.
- K. M., & Sarioglu, A. F. (2019). Combinatorial Immunophenotyping of Cell Populations with an Electronic Antibody Microarray. *Small*, 15(51).
- Liu, R., Waheed, W., Wang, N., Civelekoglu, O., Boya, M., Chu, C. H., & Sarioglu, A. F.
- 32 (2017). Design and modeling of electrode networks for code-division multiplexed resistive pulse sensing in microfluidic devices. *Lab on a Chip*, 17(15), 2650–2666.
- Liu, R., Wang, N., Kamili, F., & Sarioglu, A. F. (2016). Microfluidic CODES: A scalable
- 35 multiplexed electronic sensor for orthogonal detection of particles in microfluidic channels.
- 36 Lab on a Chip, 16(8), 1350–1357.
- Liu, Y., Germain, T., & Pappas, D. (2014). Microfluidic antibody arrays for simultaneous cell separation and stimulus. *Analytical and Bioanalytical Chemistry*, 406(30), 7867–7873.
- 39 M Weerakoon-Ratnayake, K., Vaidyanathan, S., Larky, N., Dathathreya, K., Hu, M., Jose, J.,
- 40 Mog, S., August, K., K Godwin, A., L Hupert, M., A Witek, M., & A Soper, S. (2020).
- 41 Microfluidic Device for On-Chip Immunophenotyping and Cytogenetic Analysis of Rare
- 42 Biological Cells. *Cells*, 9(2).

- Mishra, A., Gupta, M., Dalvi, A., Ghosh, K., & Madkaikar, M. (2014). Rapid flow cytometric
 prenatal diagnosis of primary immunodeficiency (PID) Disorders. *Journal of Clinical Immunology*, 34(3), 316–322.
- Overgaard, N. H., Jung, J.-W., Steptoe, R. J., & Wells, J. W. (2015). CD4 + /CD8 + double-positive T cells: more than just a developmental stage? *Journal of Leukocyte Biology*, 97(1), 31–38.
- Priyadarssini, M., Divya Priya, D., Indhumathi, S., Rajappa, M., Chandrashekar, L., & Thappa,
 D. M. (2016). Immunophenotyping of T cells in the peripheral circulation in psoriasis.
 British Journal of Biomedical Science, 73(4), 174–179.
- Qasaimeh, M. A., Wu, Y. C., Bose, S., Menachery, A., Talluri, S., Gonzalez, G., Fulciniti, M.,
 Karp, J. M., Prabhala, R. H., & Karnik, R. (2017). Isolation of Circulating Plasma Cells in
 Multiple Myeloma Using CD138 Antibody-Based Capture in a Microfluidic Device.
 Scientific Reports, 7.
- Rebecca Grant, K. C. N. M. S. S.-G. J. J. C. B. K. J. B. and J. P. (2021). Quantifying Operator Subjectivity within Flow Cytometry Data Analysis as a Source of Measurement Uncertainty and the Impact of Experience on Results. *PDA Journal of Pharmaceutical Science and Technology*, 75(1), 33–47.
- Saeys, Y., van Gassen, S., & Lambrecht, B. N. (2016). Computational flow cytometry: Helping to make sense of high-dimensional immunology data. *Nature Reviews Immunology*, 16(7), 449–462.
- Spec, A., Shindo, Y., Burnham, C. A. D., Wilson, S., Ablordeppey, E. A., Beiter, E. R., Chang,
 K., Drewry, A. M., & Hotchkiss, R. S. (2016). T cells from patients with Candida sepsis
 display a suppressive immunophenotype. *Critical Care*, 20(1).
- Trusler, O., Huang, Z., Goodwin, J., & Laslett, A. L. (2018). Cell surface markers for the identification and study of human naive pluripotent stem cells. *Stem Cell Research*, 26, 36–43.
- Vickers, D. A. L., Chory, E. J., & Murthy, S. K. (2012). Separation of two phenotypically similar cell types via a single common marker in microfluidic channels. *Lab on a Chip*, 12(18), 3399–3407.
- Wang, N., Liu, R., Asmare, N., Chu, C. H., Civelekoglu, O., & Sarioglu, A. F. (2021). Closed loop feedback control of microfluidic cell manipulation: Via deep-learning integrated sensor
 networks. *Lab on a Chip*, 21(10), 1916–1928.
- Wang, N., Liu, R., Asmare, N., Chu, C. H., & Sarioglu, A. F. (2019). Processing code multiplexed Coulter signals: Via deep convolutional neural networks. *Lab on a Chip*,
 19(19), 3292–3304.
- Watkins, N. N., Hassan, U., Damhorst, G., Ni, H. K., Vaid, A., Rodriguez, W., & Bashir, R.
 (2013). Microfluidic CD4+ and CD8+ T lymphocyte counters for point-of-care HIV diagnostics using whole blood. *Science Translational Medicine*, 5(214).
- Zhang, Y., Zhou, Y., Li, W., Lyons, V., Johnson, A., Venable, A., Griswold, J., & Pappas, D.
 (2018). Multiparameter Affinity Microchip for Early Sepsis Diagnosis Based on CD64 and
 CD69 Expression and Cell Capture. *Analytical Chemistry*, 90(12), 7204–7211.
- Zola, H., Swart, B., Banham, A., Barry, S., Beare, A., Bensussan, A., Boumsell, L., D. Buckley,
 C., Bühring, H. J., Clark, G., Engel, P., Fox, D., Jin, B. Q., Macardle, P. J., Malavasi, F.,

Mason, D., Stockinger, H., & Yang, X. (2007). CD molecules 2006 - Human cell differentiation molecules. *Journal of Immunological Methods*, 319(1–2), 1–5.

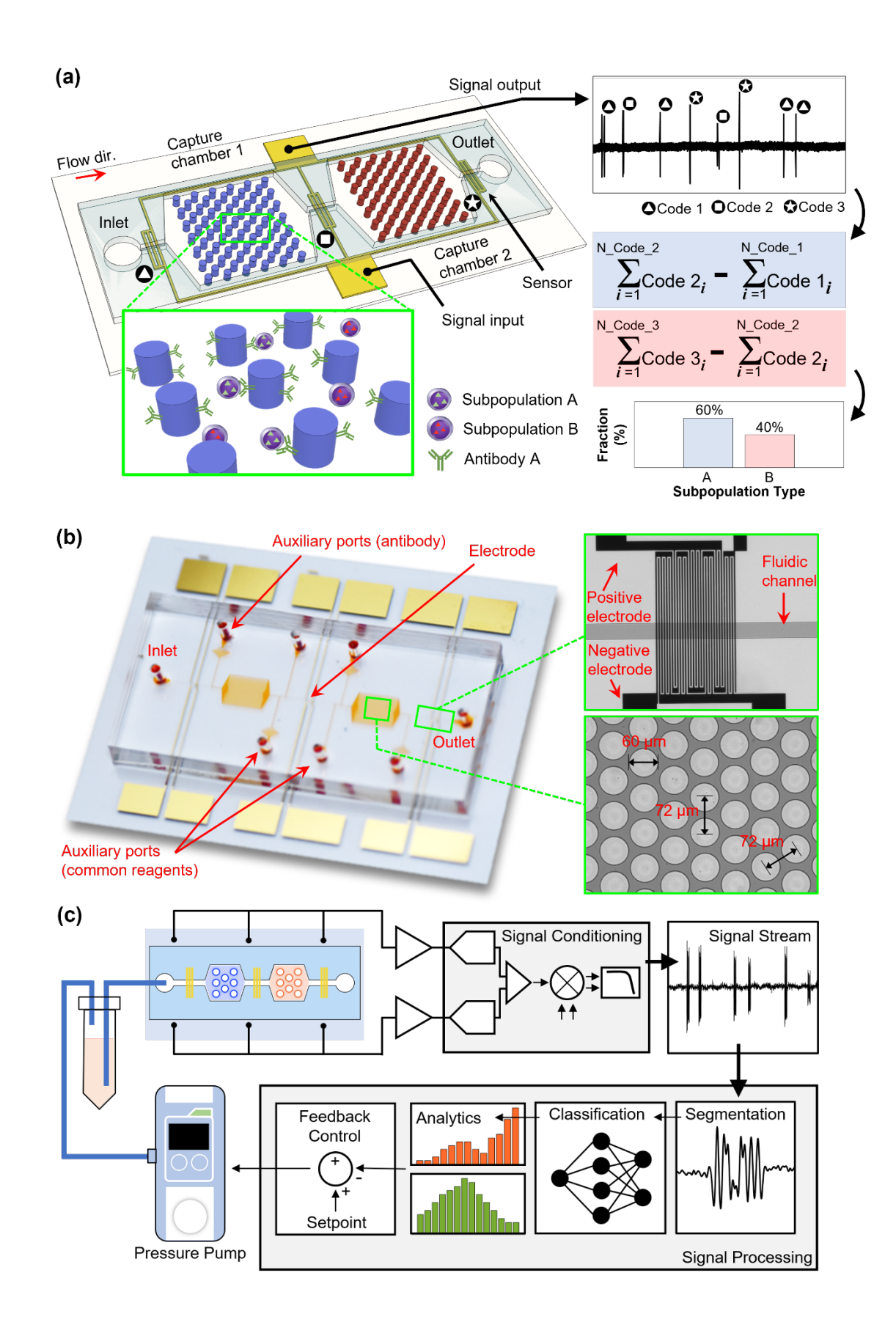


Fig. 1. Device and system overview. (a) A schematic illustrating the method for electronic immune cell analysis. The drawing shows the placement of the antibody-functionalized capture chambers on the microchip, the integrated barcoded sensor network that performs the transduction of cell surface expression into electrical signals. The signal stream is subsequently processed to match the barcode with the on-chip location where the cell event occurred and aggregated to compute the total count of cells captured in each chamber to yield population-level insights based on their surface biomarkers. (b) A photograph of the fabricated microchip showing the microfluidic features filled with red dye for visualization and the electrical sensor network formed by micropatterned gold electrodes. Insets show a close-up microscope image of (top) one of the coded electrical sensors on the device along with the inter-chamber microfluidic passage it monitors and (bottom) a group of micropillars within the capture chamber that cells interact with as they flow through the device. (c) A schematic showing all of the components of the developed autonomous microchip-based immunoassay system and their interaction.

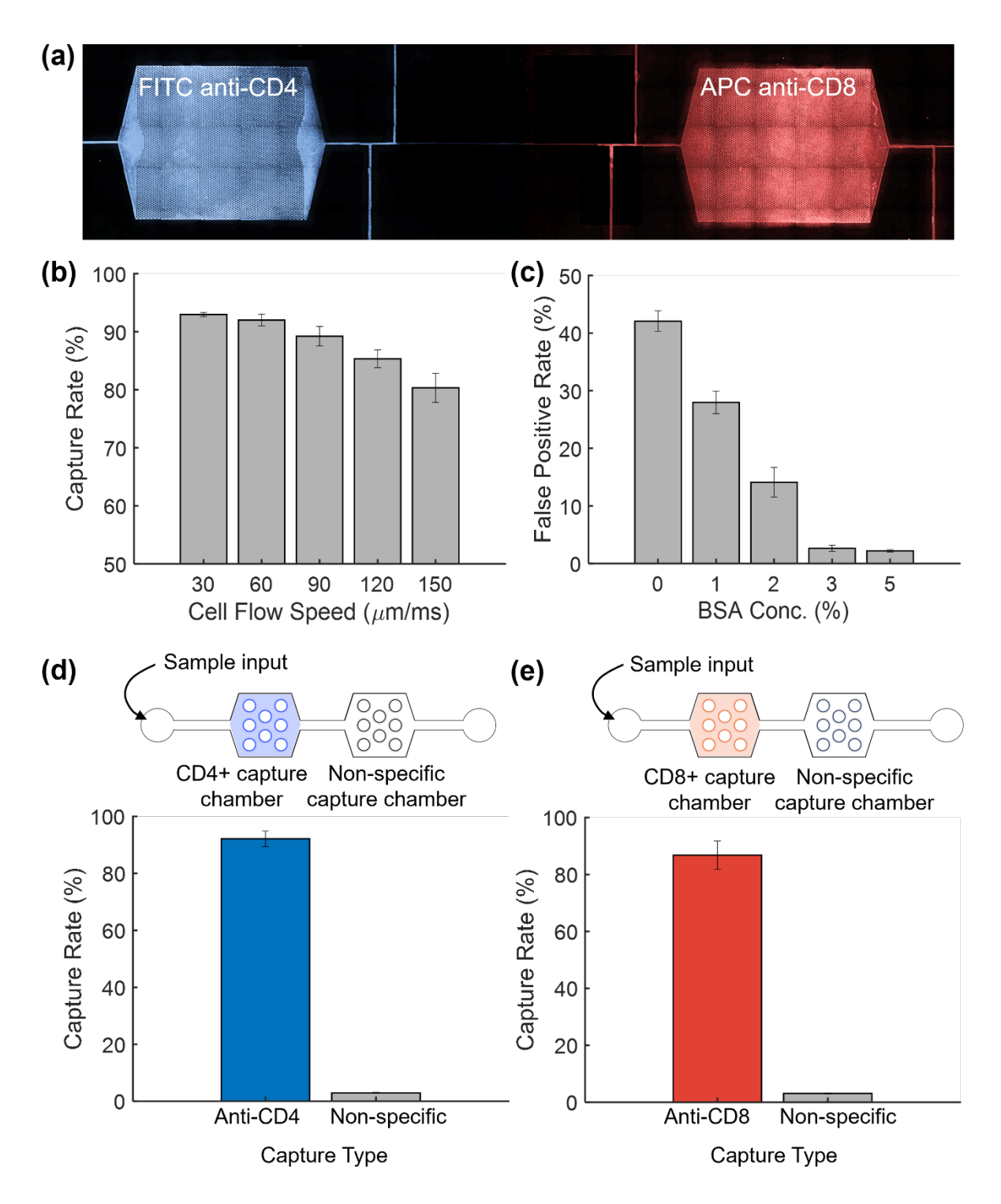


Fig. 2. Optimization and characterization of device functionalization. (a) A fluorescence microscope image showing a device whose chambers were functionalized with fluorophore-conjugated antibodies (FITC anti-CD4 (left) and APC anti-CD8 (right)). Each chamber exclusively contained the intended capture antibody. (b) Measured CD4+ T cell capture rate in a device functionalized with anti-CD4 antibodies as a function of cell flow speed. (c) Measured false positive rate (i.e., rate of non-specific cell capture) as a function of concentration of BSA

solution used to block the device. Schematics showing the functionalization layouts of analytical devices that have only one of their two chambers functionalized with (d) anti-CD4 antibody and (e) anti-CD8 antibody (top) and the measured specific (1st chamber) and non-specific (2nd chamber) cell capture rates in those devices (bottom).

1 2

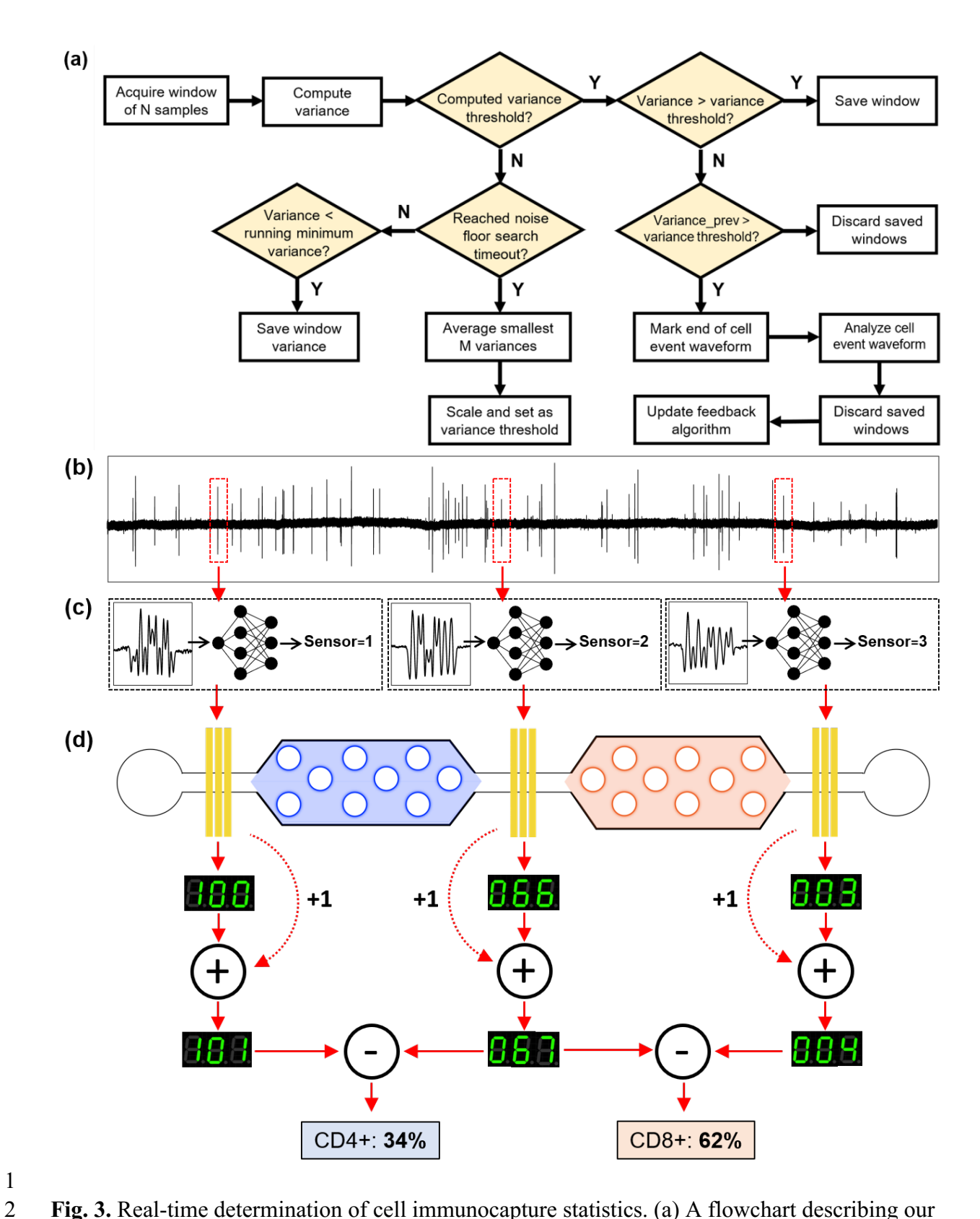


Fig. 3. Real-time determination of cell immunocapture statistics. (a) A flowchart describing our algorithm that extracted relevant events from the signal stream and passed it along to the

subsequent stage in the data processing pipeline in real-time. (b) A representative portion of a sampled signal stream produced at the output of the signal conditioning stage. (c) Cell detection signals from three different sensors segmented from the signal stream for further processing. Deep neural networks are used for localization and classification. (d) A schematic depicting the process to compute the capture rates in individual chambers. All the sensor ID outputs of the classifier network were timestamped and matched to the physical sensor location they were sourced from. This was used to calculate how many cells entered a chamber, and how many exited from it, and ultimately the capture rate of both chambers.

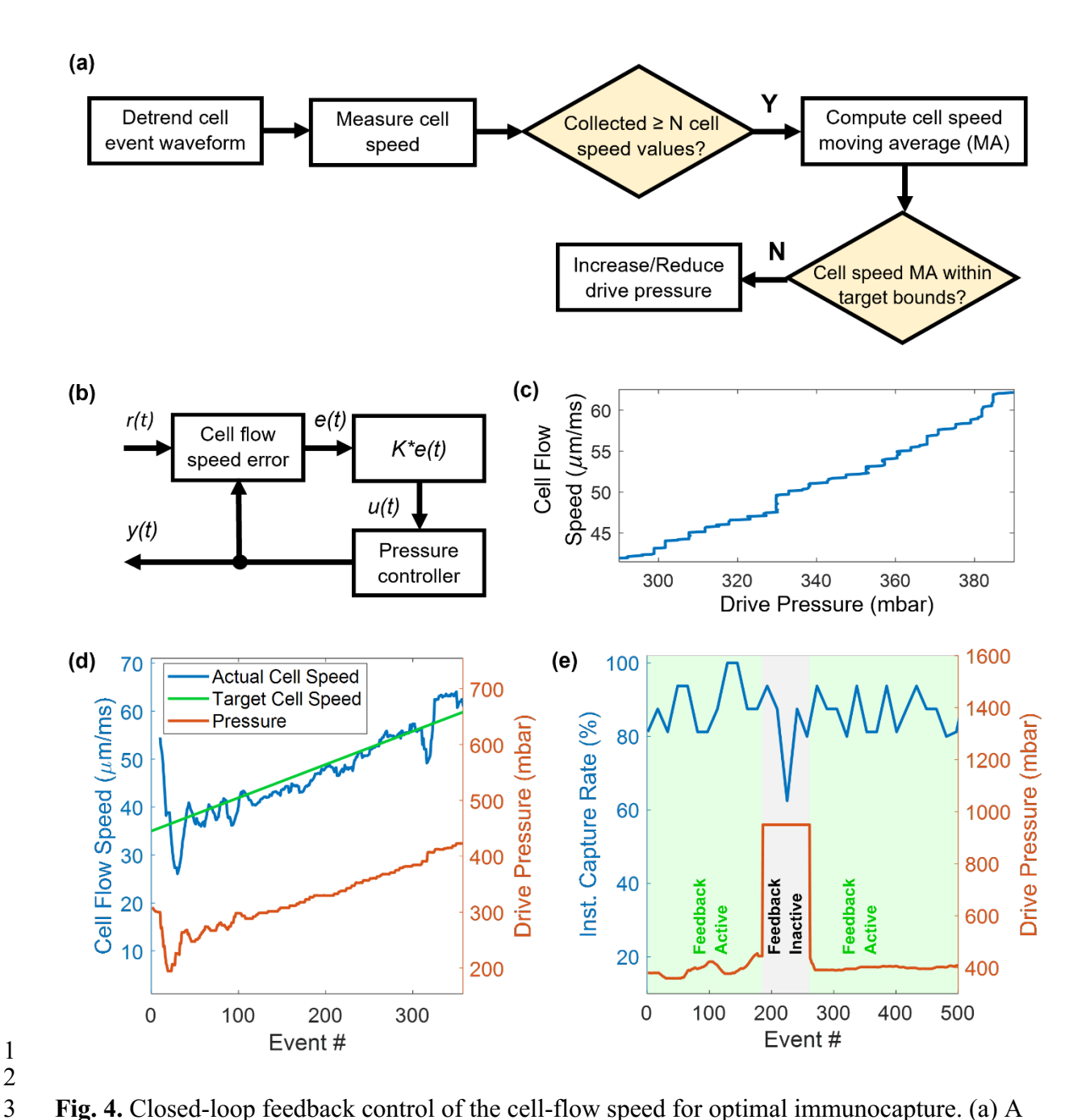


Fig. 4. Closed-loop feedback control of the cell-flow speed for optimal immunocapture. (a) A flowchart describing the feedback control algorithm. (b) A block diagram showing the proportional controller implemented in the real-time feedback control algorithm. The error term, e(t), was multiplied by the feedback gain parameter to produce the corrective drive pressure value, u(t), used to update the pressure pump. (c) A plot showing the measured cell flow speed as a function of the drive pressure in our device. (d) A plot showing the target tracking performance of our feedback controller. As the target cell speed was continuously ramped, the pressure updates commanded by the feedback controller and the resulting cell speed were simultaneously recorded and shown in the plot. (e) A plot showing the instantaneous cell immunocapture rates during both the presence and absence of feedback control. Feedback control was disabled and

drive pressure was increased to simulate an external perturbation. The consequent dip in the cell capture rate observed during inactive feedback control recovered when the feedback was turned back on.

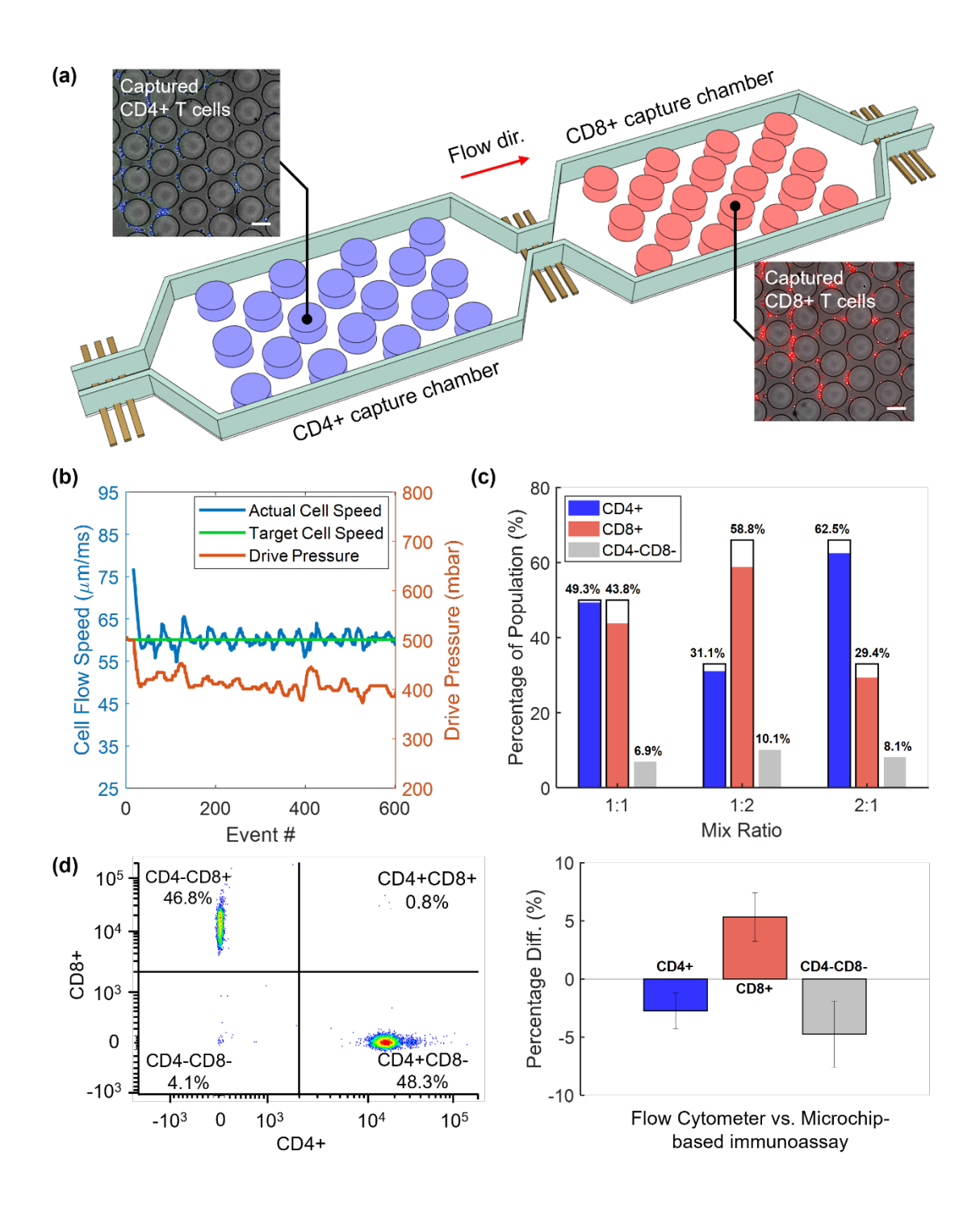


Fig. 5. Immunoanalysis of heterogenous T cell populations. (a) A schematic of the device showing the layout of capture chambers designed to capture CD4+ and CD8+ T cells and the sensors monitoring cell capture. Insets show images of CD4+ (left) and CD8+ (right) cells labeled fluorescently after they were captured on the device. Scale bar, 50 μ m. (b) A plot showing the time evolution of the cell flow speed under feedback control modulating the drive

pressure to reach the prescribed target of $60~\mu m/ms$. (c) A plot showing the CD4+ and CD8+ T cell subpopulation frequencies as reported by our system (color-filled bars) vs the nominal mix ratio determined by hemocytometer (unfilled bars). (d) A plot (left) showing the results from fluorescence-emission based classification of a sample made of equal parts CD4+ and CD8+ T cells using flow cytometry. The other plot (right) shows the difference between the subpopulation counts determined by flow cytometry vs. our microchip-based immunoassay.